Thermal-strain-engineered ferromagnetism of $LaMnO_3/SrTiO_3$ heterostructures grown on silicon

Binbin Chen [1], Nicolas Gauquelin [2], Pim Reith [1], Ufuk Halisdemir [1], Daen Jannis [2], Matjaž Spreitzer [3], Mark Huijben [1], Stefan Abel [4], Jean Fompeyrine [4], Johan Verbeeck [2], Hans Hilgenkamp [1], Guus Rijnders [1], and Gertjan Koster [1,*]

[1] *MESA+ Institute for Nanotechnology, University of Twente, 7500 AE Enschede, The Netherlands*
[2] *Electron Microscopy for Materials Science (EMAT), University of Antwerp, 2020 Antwerp, Belgium*
[3] *Advanced Materials Department, Jožef Stefan Institute, 1000 Ljubljana, Slovenia*
[4] *IBM Research-Zurich, 8803 Rüschlikon, Switzerland*

(Received 24 October 2019; revised manuscript received 19 December 2019; accepted 17 January 2020; published 12 February 2020)

The integration of oxides on Si remains challenging, which largely hampers the practical applications of oxide-based electronic devices with superior performance. Recently, $LaMnO_3/SrTiO_3$ (LMO/STO) heterostructures have gained renewed interest for the debating origin of the ferromagnetic-insulating ground state as well as for their spin-filter applications. Here we report on the structural and magnetic properties of high-quality LMO/STO heterostructures grown on silicon. The chemical abruptness across the interface was investigated by atomic-resolution scanning transmission electron microscopy. The difference in the thermal expansion coefficients between LMO and Si imposed a large biaxial tensile strain to the LMO film, resulting in a tetragonal structure with $c/a \sim 0.983$. Consequently, we observed a significantly suppressed ferromagnetism along with an enhanced coercive field, as compared to the less distorted LMO film ($c/a \sim 1.004$) grown on STO single crystal. The results are discussed in terms of tensile-strain enhanced antiferromagnetic instabilities. Moreover, the ferromagnetism of LMO on Si sharply disappeared below a thickness of 5 unit cells, in agreement with the LMO/STO case, pointing to a robust critical behavior irrespective of the strain state. Our results demonstrate that the growth of oxide films on Si can be a promising way to study the tensile-strain effects in correlated oxides, and also pave the way towards the integration of multifunctional oxides on Si with atomic-layer control.

DOI: 10.1103/PhysRevMaterials.4.024406

I. INTRODUCTION

Strain-related approaches have been extensively explored to engineer oxide functionalities over the past few decades [1]. Typical examples include the tensile-strain induced room-temperature ferroelectricity in $SrTiO_3$ (STO) and emergent multiferroicity in $EuTiO_3$ [2,3], doubled superconducting critical temperatures in compressively strained $La_{1.9}Sr_{0.1}CuO_4$ [4], tunable phase separation in colossal magnetoresistive (CMR) manganites [5], and tailored two-dimensional electron gases (2DEGs) at the $LaAlO_3$/STO interface [6]. Normally, the strain is applied by growing epitaxial oxide films on substrates with different lattice parameters. In this way large static strain can be achieved, well above the amount that causes fractures in bulk materials [1]. Piezoelectric substrates are also used to dynamically tune such an epitaxial strain by applying voltage [7]. In such epitaxial films, as the thickness increases above a critical value, it becomes energetically favorable to introduce dislocations to release the elastic strain energy [8]. Therefore strain effects in thick films are limited. Aside from the epitaxial strain, bending devices are designed to impart mechanical strain to oxide films with larger lateral dimensions [9]. Furthermore, using thermal strain can be an alternative by taking advantages of the difference in the thermal expansion coefficients (TEC) between the film and substrate [10,11]. In the case of oxide films grown on silicon, tensile strains are usually generated in the films after cooling down from the growth temperature. The strain arises from the clamping effect of Si which shows a significantly smaller TEC $\sim 2.6 \times 10^{-6}/^{\circ}C$ as compared to oxides [11–13]. Given the limited choice of commercially available single-crystal substrates, especially those with large lattice parameters, the integration of oxides on silicon offers an additional path to examine the tensile strain effects in oxide films.

As the parent compound of CMR manganites, $LaMnO_3$ (LMO) has aroused renewed interests spurred by the debating origin of the ferromagnetism (FM) in its thin-film form [14–23]. In bulk LMO, the Jahn-Teller distortions of Mn^{3+} ions lift the degeneracy of e_g orbitals, leading to a Mott insulating state with a staggered $d_{3x^2-r^2}/d_{3y^2-r^2}$ orbital order. The superexchange interactions between Mn^{3+} result in an *A*-type antiferromagnetism [24]. By contrast, FM is observed in thick LMO films grown on STO and sharply disappears for thicknesses below 6 unit cells (ucs) [14,16]. This is reminiscent of the critical behavior of 2DEG at the $LaAlO_3$/STO interface and explained by an analogous model based on the polar discontinuity [14,25]. In that picture, owing to the relatively small band gap of LMO (~1.3 eV) compared to STO (~3.2 eV) [14], the electrons from the surface cannot transfer across the interface to the STO side, but reside at the interfacial LMO layers. Such a self-doping process turns LMO into a ferromagnetic state. However, the model cannot

*g.koster@utwente.nl

 ©2020 American Physical Society

explain the FM observed in LMO films grown on the isopolar $LaAlO_3$ substrates [16,20]. It is also argued that the FM in LMO films originates from the Mn^{3+}-O-Mn^{4+} double exchange mechanism, where the Mn^{4+} ions are produced by oxygen excess accompanied with cation deficiencies [26–29]. Along this line, the absence of FM in the ultrathin films is ascribed to a notorious "dead layer" effect, probably resulting from the accumulation of Mn^{2+} [16,17]. In both scenarios, the valence change of Mn ions plays a decisive role. On the other hand, first-principle studies reveal that compressive strain is the dominant factor stabilizing the FM in LMO films [21–23]. This is consistent with the observations in LMO films grown on commonly used substrates, including STO, $LaAlO_3$, and $(LaAlO_3)_{0.3}(Sr_2AlTaO_6)_{0.7}$(LSAT) [16,19,20]. To further validate the theoretical model, studies on tensile-strained LMO are required. Here, we investigate the FM of LMO/STO heterostructures grown on Si substrates, which show the same polar mismatch and interfacial chemistry but exhibit distinctly different strain states as compared to the widely studied LMO films grown on STO single crystals. The large difference in TEC between LMO and Si imposes a biaxial tensile strain to LMO and boosts the antiferromagnetic instabilities. As a results, the film shows a significantly suppressed magnetization but enhanced coercive field with respect to the corresponding LMO film on STO. Moreover, LMO films on Si show the same critical thickness (∼ 6 uc) for FM as the LMO/STO case, pointing to a universal character irrespective of the strain states.

II. METHODS

The LMO films were fabricated through a pulsed laser deposition (PLD) method *in situ* monitored by reflection high energy electron diffraction (RHEED). Prior to the deposition of LMO film, a 10-uc-thick STO buffer layer was deposited by molecular beam epitaxy (MBE) for which the details can be found elsewhere [30]. The LMO films were ablated from a polycrystalline LMO target at 750 °C under an oxygen pressure of 0.01 mbar. The laser fluence and repetition rate were set at $2\,J/cm^2$ and 2 Hz, respectively. The surface morphology was examined using atomic force microscopy (AFM). The crystal structure was characterized by high-resolution x-ray diffraction (XRD) including reciprocal space mappings (RSMs). The atomic structure across the LMO/STO interface was characterized by Cs-corrected scanning transmission electron microscopy (STEM) high angle annular dark field (HAADF) imaging on the X-Ant-Em instrument operated at 300 kV. The bulk magnetic properties were measured through vibrating sample magnetometry on a Quantum Design physical property measurement system. Scanning superconducting quantum interference device microscopy (SSM) was employed to characterize the magnetism within LMO films at the microscale.

III. RESULTS AND DISCUSSION

Figure 1(a) shows RHEED intensity oscillations of LMO films on Si with various thicknesses ranging from 5 to 20 uc.

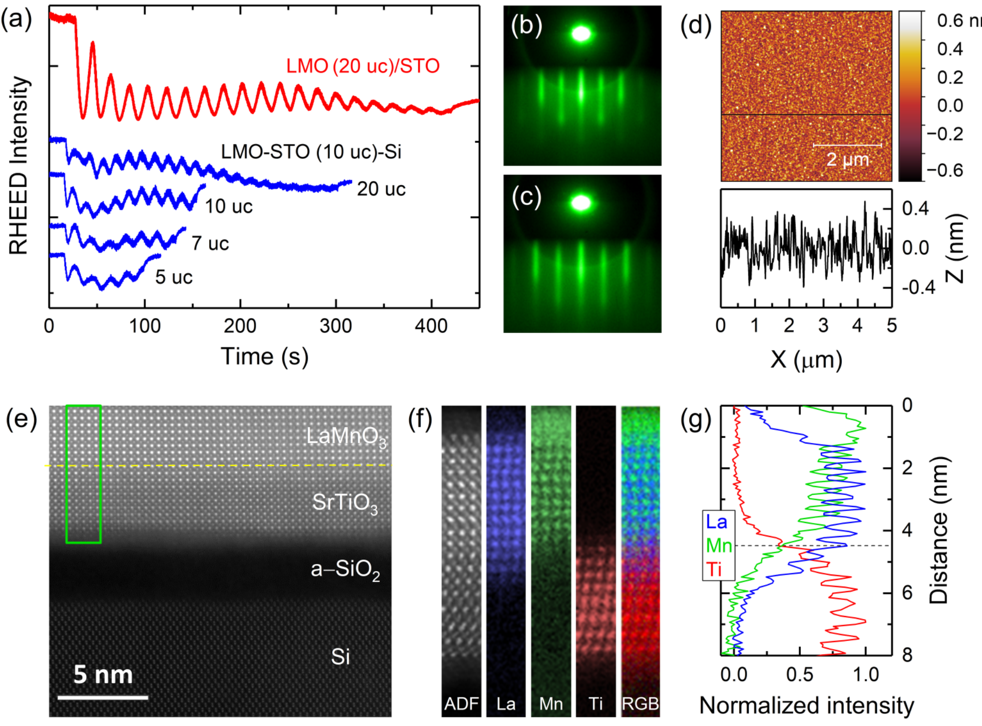

FIG. 1. (a) RHEED intensity oscillations for LMO films grown on a STO single crystal (red line) and STO-buffered Si substrates (blue lines). (b), (c) RHEED patterns recorded before and after the deposition of 10-uc LMO on Si. (d) AFM image of a 10-uc LMO film on STO-buffered Si. The bottom panel shows the height profile along the dotted line in the AFM image. (e) Cross-sectional HAADF-STEM image of a 10-uc LMO film on STO-buffered Si. (f) HAADF and EELS elemental maps (La, Mn, Ti and RGB mix) taken from the area marked by the green box in (e). (g) Layer-resolved EELS intensities of La (blue), Mn (green) and Ti (red) across the LMO/STO interface. The nominal interface position is indicated by the dotted line.

The profile of a 20-uc LMO film grown on TiO_2-terminated STO is also shown as a benchmark. All films on silicon clearly show the layer-by-layer growth mode, comparable with the LMO/STO film. Figures 1(b) and 1(c) show the RHEED patterns recorded before and after the growth of 10-uc LMO on Si. The streaky features attest to the smooth surface of both the STO buffer layer and the LMO film. The surface morphology is further checked by AFM for the 10-uc LMO film as shown in Fig. 1(d). A rms roughness of ∼1.7 Å is obtained, which is on par with the best oxide films on Si grown by MBE [13]. To further characterize the interfacial structure at the atomic level, we performed STEM-HAADF measurements on a 10-uc LMO film on Si as shown in Figs. 1(e)–1(g). An amorphous SiO_2 layer of ∼5 nm is formed in between the STO layer and the Si substrate [Fig. 1(e)], which mostly originates from the oxygen diffusion from STO to Si during the deposition of LMO at high temperature and oxygen atmosphere [11–13]. Note that the formation of this interfacial layer occurs after the epitaxial relationship between the perovskite and silicon is set, as proved by our XRD φ scans shown below. Importantly, the LMO film is free of defects and perfectly coherent with the STO buffer layer, demonstrating the high crystallinity. The chemical profile across the LMO/STO interface was investigated by electron energy loss spectroscopy (EELS) elemental maps measured at Ti $L_{2,3}$, Mn $L_{2,3}$ and La $M_{4,5}$ edges. As can be seen from Figs. 1(f) and 1(g), the La ions from LMO diffuse ∼2 uc deep into the STO layer, but no evident intermixing between Mn and Ti has been detected across the interface, consistent with the previous study on LMO/STO heterostructures [18]. The chemically abrupt interface as well as the two-dimensional growth mode achieved on Si by PLD will benefit the further integration of oxide heterostructures and superlattices on Si with atomic-layer control.

Figure 2(a) shows the XRD θ-2θ scans of 20-uc LMO films grown on STO and Si. No secondary phases can be detected and only $(00l)$ peaks are observed, indicative of the phase-pure and single oriented film on Si. The presence of thickness fringes for both samples again confirms the sharp interfaces and smooth surfaces. For the LMO/STO film, the film peak almost superimposes with the substrate peak, implying the closely matched crystal lattice. The XRD simulation reveals an out-of-plane lattice constant of $c = 3.923 \pm 0.004$ Å (pseudocubic lattice constants are used in this paper) [31], which is much larger than the corresponding film on Si with $c = 3.879$ Å. It has been reported that the large difference in c can be caused by the varied oxygen content in the films [26–28]. However, this can be overestimated by considering the identical oxygen pressure and thermal history during the deposition of both films. Hence, the results point to the distinct strain states for LMO grown on STO and Si. To confirm the epitaxial relationship, we conducted the XRD φ scans around the Si (220) and LMO $(110)_{pc}$ peaks as shown in Fig. 2(b). It is evident that the four peaks of Si locate 45° apart from the peaks of LMO. This implies the LMO primitive lattice rotates 45° with respect to the underlying Si, as schematically drawn in the inset of Fig. 2(b).

To further compare the strain states in the two films, we measured the RSMs around the asymmetric $(103)_{pc}$ Bragg reflections of LMO at four different φ angles as shown in

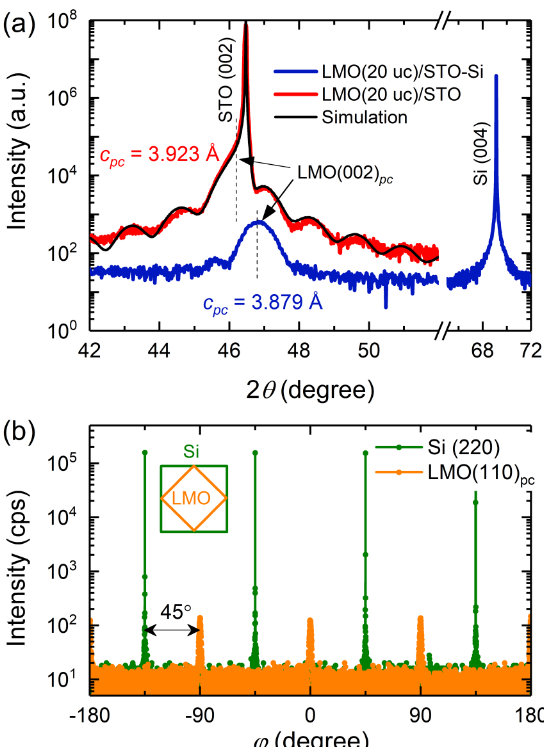

FIG. 2. (a) High-resolution XRD θ-2θ scans of 20-uc LMO films grown on the STO and STO-buffered Si substrates. Simulated XRD pattern yields an out-of-plane lattice constant $c_{pc} = 3.923 \pm 0.004$ Å for the LMO/STO film. (b) φ scans around Si (220) and LMO $(110)_{pc}$ peaks. The epitaxial relationship is schematically drawn in the inset.

Fig. 3. When grown on STO [Fig. 3(a)], the LMO film is coherently strained to the substrate as indicated by their identical Q_X value, yielding an in-plane lattice constant $a = 3.905$ Å. The four reflections from LMO show the same Q_Z values, which means the film adopts a tetragonal structure. The c/a ratio can be calculated as 1.004, attesting to the slightly compressive strain. For the film grown on Si as shown in Fig. 3(b), the reflections show a broad feature because of the in-plane mosaic spread [13]. Analogous to the LMO/STO film, a tetragonally distorted structure is also deduced for LMO grown on Si. By projecting the reflections to the Q_X and Q_Z axes, a and c can be calculated as 3.94 and 3.874 Å, respectively. Thus the tensile strain gives rise to a c/a ratio of ∼0.983, suggesting a significantly stronger tetragonal distortion than the LMO/STO case. Such a tensile strain cannot be induced by the lattice mismatch given the relatively small lattice spacing along Si [110] (∼3.84 Å). Instead, we ascribe it to the mismatch in the thermal expansion coefficients between Si ($\alpha_{Si} = 2.6 \times 10^{-6}$/°C) and LMO ($\alpha_{LMO} = 11.2 \times 10^{-6}$/°C) [32]. Stoichiometric LMO in its bulk form shows a *Pbnm* orthorhombic structure with a pseudocubic lattice constant of ∼3.936 Å [26]. In its thin-film form, the volume of unit cell can be different because oxygen excess and cation deficiency are usually involved [29,33]. Therefore we first extract the lattice constant of strain-free LMO based on the XRD data of LMO/STO film using the Poisson equation:

$$c = \frac{2\nu}{\nu - 1}a + \frac{1+\nu}{1-\nu}a_0,$$

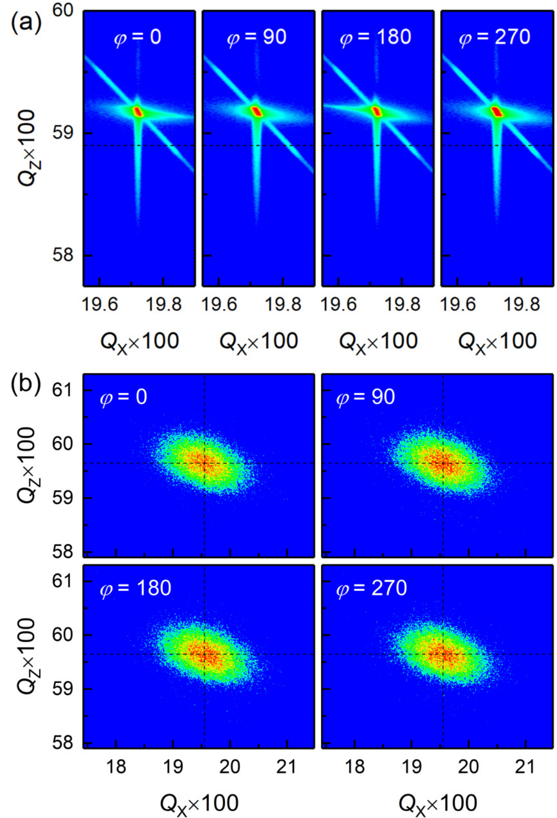

FIG. 3. RSMs around the $LMO(103)_{pc}$ reflection at four different φ angles measured from the 20-uc LMO films grown on STO (a) and STO-buffered Si (b) substrates.

where ν and a_0 are the Poisson ratio and bulk lattice constant of LMO, respectively. a_0 is calculated to be 3.915 Å using $a = 3.905$ Å, $c = 3.923$ Å and $\nu = 0.3$ [34]. Assuming LMO is fully relaxed at the growth temperature ($T_g = 750\,^{\circ}$C), the lattice constant of LMO at T_g is calculated as: $a_{T_g} = a_0 + a_0\alpha_{\rm LMO}(T_g - T_0) = 3.946$ Å, where $T_0 = 30\,^{\circ}$C. As the film is cooled down from T_g to T_0, the lattice shrinkage of LMO follows the underlying Si substrate due to the clamping effect, then the room-temperature lattice constant of LMO film on Si can be calculated as: $a_{T_0} = a_{T_g} - a_{Si}\alpha_{Si}(T_g - T_0)/\sqrt{2} = 3.939$ Å using $a_{\rm Si} = 5.431$ Å. This value is in excellent agreement with that obtained from RSMs, confirming the thermal origin of the tensile strain.

We now focus on the thermal-strain effects on the magnetic properties of LMO films. Figure 4(a) shows the temperature dependent magnetization curves for a set of LMO films on Si as well as a 20-uc LMO film on STO for comparison. The samples were first cooled down to 10 K in a magnetic field of 1 T, then an in-plane field of 1000 Oe was applied and the data were collected during the heating up. For the films on Si, as the thickness is reduced, both the Curie temperature (T_C) and magnetization at low temperature decrease and suddenly disappear at 5 uc. The degraded FM is also evident from the magnetic hysteresis loops shown in Fig. 4(b). The saturation magnetization decreases from 1.4 μ_B/Mn at 20 uc to 0.5 μ_B/Mn at 7 uc, before vanishing at 5 uc. Note that the small magnetic moment of the 7-uc LMO film cannot be ascribed to the spin canting effect caused by the Dzyaloshinskii-Moriya interaction, which yields a tiny magnetic moment of $\sim$0.1 μ_B/Mn in the bulk antiferromagnetic LMO [24]. The thickness-dependent properties are in line with previous reports on the LMO/STO films [14,16,17]. In particular, unlike the TiO_2-terminated STO substrates, the surface of STO buffer layer on Si is randomly terminated by TiO_2 and SrO. Also, the LMO films on Si are tensile strained in contrast to the compressively strained LMO/STO films. Therefore, the critical behavior of FM in LMO films is robust against the substrate terminations and strain states.

We also compare the FM of 20-uc LMO films grown on STO and Si in Figs. 4(a) and 4(b). In spite of the similar $T_C \sim$ 150 K, the magnetization is drastically suppressed in the LMO film on Si, which is nearly half of the value of the LMO/STO film. The magnetic contrast can be further visualized by the SSM measurements, which probe the stray fields generated by magnetic domains using a pick-up loop [14,15]. As shown in Figs. 4(c) and 4(d), both films show patterns with randomly distributed regions having positive and negative stray fields. The rms value of the SSM signal is $\sim$2.61 μT for the LMO on Si, remarkably weaker than $\sim$9.95 μT for the LMO/STO film. At first glance, the weakened FM can be related to the mixed surface terminations of the STO buffer layer which may influence the electronic reconstructions [14,17]. However, it is found that the LMO film grown on the as-received STO substrate shows a slightly reduced saturation magnetization of $\sim$2.44 μ_B/Mn, which is $\sim$93% of the corresponding film grown on the single-terminated STO. This means the surface termination of STO plays a minor role in the FM of the overlying LMO. Instead, we attribute the large difference in the magnetization between LMO films grown on STO and Si to the different tetragonal distortions in the two films. For manganites, the strong electron-phonon coupling has been well documented, which provides a sensitive response of the electronic and magnetic phases to subtle structural perturbations [22,24,35–39]. According to first-principles calculations, a small c/a ratio can turn ferromagnetic manganites into an A-type antiferrmagnetic state by populating the occupations of $d_{x^2-y^2}$ orbitals as well as enhancing the Jahn-Teller distortions [22,36]. Experimentally, $La_{0.5}Sr_{0.5}MnO_3$ film grown on the lattice-matched LSAT substrate shows a $c/a \sim 0.99$ and robust FM, but those on STO with larger lattice constants show a smaller $c/a \sim 0.98$ and an antiferromagnetic behavior [38]. Also, the coexistence of ferromagnetic and antiferromagnetic phases has been claimed in $La_{0.7}Ca_{0.3}MnO_3$/STO film having a $c/a \sim 0.975$ [39]. Along this line, the suppressed FM of LMO film on Si can be attributed to tensile-strain-induced antiferromagnetic instabilities, which are much weakened in the less distorted LMO/STO film with $c/a \sim 1.004$. The argument is supported by the different magnetic switching behaviors of the two films shown in Fig. 4(b). While the LMO/STO film shows a slim loop with a small coercive field of $\sim$200 Oe, the film on silicon shows a sheared loop with a strongly enhanced coercive field of $\sim$1000 Oe. This means the magnetization reversal is mainly governed by the nucleation of reversed domains in the LMO/STO film but limited by the domain wall motions in the LMO film on silicon. The pinning of domain walls by the antiferromagnetic phases leads to the enhancement of coercive field [39,40].

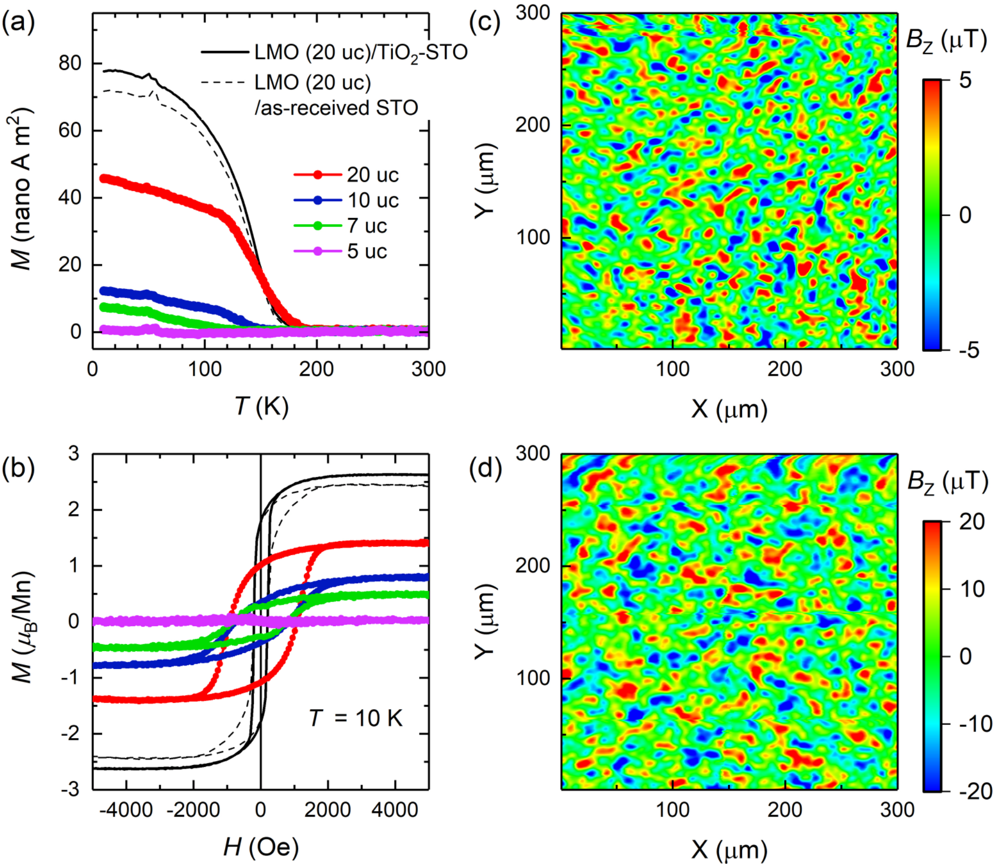

FIG. 4. (a) Temperature dependent magnetization curves of LMO films on STO-buffered Si with various thicknesses. The 20-uc LMO films on TiO_2-terminated and as-received STO substrates are included for comparison. The corresponding magnetic hysteresis loops at 10 K are shown in (b). (c) and (d) show the SSM images taken from 20-uc LMO films grown on Si and TiO_2-terminated STO, respectively. The measurements were performed at 4.2 K and zero magnetic fields. Note the difference in the scale bar of intensity.

The results are consistent with the observations on LMO/STO films grown at various oxygen pressures, where the increase of antiferromagnetic phases in LMO deposited at reduced atmosphere gives rise to a weakened magnetization but enhanced coercive field [19,20]. Moreover, it should be noted that the large tensile strain usually suppresses the magnetization and T_C simultaneously in the hole-doped manganite films [38,41,42]. However, in the present work, T_C hardly changes in the tensile-strained LMO film on Si, with respect to the LMO/STO film [Fig. 4(a)]. This discrepancy can be related to the possible magnetic cluster states of the LMO films [15], which is in contrast to the uniform double-exchange FM in the hole-doped manganite films.

Aside from the different tetragonal distortions, the stoichiometry of LMO films grown on STO single crystal and STO-buffered Si substrates can also be different. It has been proposed that oxygen excess accompanied by cation deficiencies usually form in LMO films to release the compressive strain from substrates, like LSAT and STO [29,33]. The resultant Mn^{4+} ions give rise to FM through the Mn^{3+}-O-Mn^{4+} double exchange interactions. Along this line, the tensile thermal strain from Si substrate will suppresses the formation of oxygen excess and cation deficiencies, yielding a more stoichiometric LMO film. Consequently, the Mn^{3+}-O-Mn^{4+} double exchange interactions are weakened since less Mn^{4+} ions are introduced. This scenario is consistent with suppressed FM of LMO films grown on STO-buffered Si substrates. However, LMO films grown on STO and STO-buffered Si substrates show similar transport behaviors (not shown), suggesting the difference in stoichiometry should not play a dominant role. Last but not least, the presence of imperfections, such as the in-plane mosaicity and possible Sr-rich antiphase boundaries in the STO buffer layer [43], may also contribute to the enhanced coercitity for LMO films grown on Si.

IV. CONCLUSION

To summarize, we studied the structural and magnetic properties of LMO films grown on Si. The thermal mismatch between Si and LMO established a large tensile strain in the LMO films, yielding a tetragonal structure with $c/a \sim 0.983$. As a result, the FM was dramatically suppressed compared to the LMO/STO film. Moreover, the FM disappeared upon reducing the film thickness down to 5 uc, in agreement with previous reports on the LMO/STO films. This means the critical behavior of FM in LMO films is robust against the substrate terminations and strain states. Finally, we would like

to point out that the growth of oxide films on Si can be an alternative way to examine the tensile strain effects in oxides, especially those with large lattice constants.

ACKNOWLEDGMENTS

This work is supported by the international M-ERA.NET project SIOX (project 4288) and the Dutch NWO DESCO program. J.V. and N.G. acknowledge funding through the GOA project "Solarpaint" of the University of Antwerp. The microscope used in this work was partly funded by the Hercules Fund from the Flemish Government. D.J. acknowledges funding from FWO project G093417N from the Flemish fund for scientific research. M.S. acknowledges funding from Slovenian Research Agency (Grants No. J2-9237 and No. P2-0091). S.A. and J.F. acknowledge support from the European Commission under Grant Agreement No. H2020-ICT-2016-1-732642 (ULPEC).

[1] D. G. Schlom, L. Q. Chen, C. J. Fennie, V. Gopalan, D. A. Muller, X. Pan, R. Ramesh, and R. Uecker, MRS Bull. **39**, 118 (2014).

[2] J. H. Haeni, P. Irvin, W. Chang, R. Uecker, P. Reiche, Y. L. Li, S. Choudhury, W. Tian, M. E. Hawley, B. Craigo, A. K. Tagantsev, X. Q. Pan, S. K. Streiffer, L.-Q. Chen, S. W. Kirchoefer, J. Levy, and D. G. Schlom, Nature (London) **430**, 758 (2004).

[3] J. H. Lee, L. Fang, E. Vlahos, X. Ke, Y. W. Jung, L. F. Kourkoutis, J. W. Kim, P. J. Ryan, T. Heeg, M. Roeckerath, V. Goian, M. Bernhagen, R. Uecker, P. C. Hammel, K. M. Rabe, S. Kamba, J. Schubert, J. W. Freeland, D. A. Muller, C. J. Fennie, P. Schiffer, V. Gopalan, E. Johnston-Halperin, and D. G. Schlom, Nature (London) **466**, 954 (2010).

[4] J.-P. Locquet, J. Perret, J. Fompeyrine, E. Mächler, J. W. Seo, and G. Van Tendeloo, Nature (London) **394**, 453 (1998).

[5] T. Z. Ward, J. D. Budai, Z. Gai, J. Z. Tischler, L. Yin, and J. Shen, Nat. Phys. **5**, 885 (2009).

[6] C. W. Bark, D. A. Felker, Y. Wang, Y. Zhang, H. W. Jang, C. M. Folkman, J. W. Park, S. H. Baek, H. Zhou, D. D. Fong, X. Q. Pan, E. Y. Tsymbal, M. S. Rzchowski, and C. B. Eom, Proc. Natl. Acad. Sci. **108**, 4720 (2011).

[7] M. D. Biegalski, K. Dörr, D. H. Kim, and H. M. Christen, Appl. Phys. Lett. **96**, 151905 (2010).

[8] M. D. Biegalski, D. D. Fong, J. A. Eastman, P. H. Fuoss, S. K. Streiffer, T. Heeg, J. Schubert, W. Tian, C. T. Nelson, X. Q. Pan, M. E. Hawley, M. Bernhagen, P. Reiche, R. Uecker, S. Trolier-McKinstry, and D. G. Schlom, J. Appl. Phys. **104**, 114109 (2008).

[9] J. M. Gregg and R. M. Bowman, Appl. Phys. Lett. **71**, 3649 (1997).

[10] H. W. Jang, S. H. Baek, D. Ortiz, C. M. Folkman, R. R. Das, Y. H. Chu, P. Shafer, J. X. Zhang, S. Choudhury, V. Vaithyanathan, Y. B. Chen, D. A. Felker, M. D. Biegalski, M. S. Rzchowski, X. Q. Pan, D. G. Schlom, L. Q. Chen, R. Ramesh, and C. B. Eom, Phys. Rev. Lett. **101**, 107602 (2008).

[11] L. Zhang, Y. Yuan, J. Lapano, M. Brahlek, S. Lei, B. Kabius, V. Gopalan, and R. Engel-Herbert, ACS Nano **12**, 1306 (2018).

[12] Z. Wang, H. Paik, Z. Chen, D. A. Muller, and D. G. Schlom, APL Mater. **7**, 022520 (2019).

[13] Z. Wang, Z. Chen, A. B. Mei, X. Bai, L. F. Kourkoutis, D. A. Muller, and D. G. Schlom, J. Vac. Sci. Technol. A **36**, 021507 (2017).

[14] X. R. Wang, C. J. Li, W. M. Lü, T. R. Paudel, D. P. Leusink, M. Hoek, N. Poccia, A. Vailionis, T. Venkatesan, J. M. D. Coey, E. Y. Tsymbal, Ariando, and H. Hilgenkamp, Science **349**, 716 (2015).

[15] Y. Anahory, L. Embon, C. J. Li, S. Banerjee, A. Meltzer, H. R. Naren, A. Yakovenko, J. Cuppens, Y. Myasoedov, M. L. Rappaport, M. E. Huber, K. Michaeli, T. Venkatesan, Ariando, and E. Zeldov, Nat. Commun. **7**, 12566 (2016).

[16] W. Niu, W. Liu, M. Gu, Y. Chen, X. Zhang, M. Zhang, Y. Chen, J. Wang, J. Du, F. Song, X. Pan, N. Pryds, X. Wang, P. Wang, Y. Xu, Y. Chen, and R. Zhang, Adv. Electron. Mater. **4**, 1800055 (2018).

[17] Z. Chen, Z. Chen, Z. Q. Liu, M. E. Holtz, C. J. Li, X. R. Wang, W. M. Lü, M. Motapothula, L. S. Fan, J. A. Turcaud, L. R. Dedon, C. Frederick, R. J. Xu, R. Gao, A. T. N'Diaye, E. Arenholz, J. A. Mundy, T. Venkatesan, D. A. Muller, L.-W. Wang, J. Liu, and L. W. Martin, Phys. Rev. Lett. **119**, 156801 (2017).

[18] M. Li, C. Tang, T. R. Paudel, D. Song, W. Lü, K. Han, Z. Huang, S. Zeng, X. R. Wang, P. Yang, Ariando, J. Chen, T. Venkatesan, E. Y. Tsymbal, C. Li, and S. J. Pennycook, Adv. Mater. **31**, 1901386 (2019).

[19] J. Roqueta, A. Pomar, L. Balcells, C. Frontera, S. Valencia, R. Abrudan, B. Bozzo, Z. Konstantinović, J. Santiso, and B. Martínez, Cryst. Growth Des. **15**, 5332 (2015).

[20] Y. Liu, H. F. Wong, K. K. Lam, C. L. Mak, and C. W. Leung, J. Magn. Magn. Mater. **481**, 85 (2019).

[21] Y. S. Hou, H. J. Xiang, and X. G. Gong, Phys. Rev. B **89**, 064415 (2014).

[22] J. H. Lee, K. T. Delaney, E. Bousquet, N. A. Spaldin, and K. M. Rabe, Phys. Rev. B **88**, 174426 (2013).

[23] M. An, Y. Weng, H. Zhang, J.-J. Zhang, Y. Zhang, and S. Dong, Phys. Rev. B **96**, 235112 (2017).

[24] I. Solovyev, N. Hamada, and K. Terakura, Phys. Rev. Lett. **76**, 4825 (1996).

[25] N. Nakagawa, H. Y. Hwang, and D. A. Muller, Nat. Mater. **5**, 204 (2006).

[26] C. Ritter, M. R. Ibarra, J. M. De Teresa, P. A. Algarabel, C. Marquina, J. Blasco, J. García, S. Oseroff, and S. W. Cheong, Phys. Rev. B **56**, 8902 (1997).

[27] W. S. Choi, Z. Marton, S. Y. Jang, S. J. Moon, B. C. Jeon, J. H. Shin, S. S. A. Seo, T. W. Noh, K. Myung-Whun, H. N. Lee, and Y. S. Lee, J. Phys. D: Appl. Phys. **42**, 165401 (2009).

[28] Q. Huang, A. Santoro, J. W. Lynn, R. W. Erwin, J. A. Borchers, J. L. Peng, and R. L. Greene, Phys. Rev. B **55**, 14987 (1997).

[29] J. M. Vila-Fungueiriño, B. Rivas-Murias, B. Rodríguez-González, O. Txoperena, D. Ciudad, L. E. Hueso, M. Lazzari, and F. Rivadulla, ACS Appl. Mater. Interfaces **7**, 5410 (2015).

[30] C. Marchiori, M. Sousa, A. Guiller, H. Siegwart, J. P. Locquet, J. Fompeyrine, G. J. Norga, and J. W. Seo, Appl. Phys. Lett. **88**, 072913 (2006).

[31] C. Lichtensteiger, J. Appl. Crystallogr. **51**, 1745 (2018).
[32] S. Srilomsak, D. P. Schilling, and H. U. Anderson, in *Proceedings of the First International Symposium on Solid Oxide Fuel Cells*, edited by S. C. Singhal (The Electrochemical Society, Pennington, NJ, 1989), Vol. 11 , pp. 129–140.
[33] I. Marozau, P. T. Das, M. Döbeli, J. G. Storey, M. A. Uribe-Laverde, S. Das, C. Wang, M. Rössle, and C. Bernhard, Phys. Rev. B **89**, 174422 (2014).
[34] J. J. U. Buch, G. Lalitha, T. K. Pathak, N. H. Vasoya, V. K. Lakhani, P. V. Reddy, R. Kumar, and K. B. Modi, J. Phys. D **41**, 025406 (2008).
[35] H. Röder, J. Zang, and A. R. Bishop, Phys. Rev. Lett. **76**, 1356 (1996).
[36] Z. Fang, I. V. Solovyev, and K. Terakura, Phys. Rev. Lett. **84**, 3169 (2000).
[37] Z. Huang, L. F. Wang, P. F. Chen, G. Y. Gao, X. L. Tan, B. W. Zhi, X. F. Xuan, and W. B. Wu, Phys. Rev. B **86**, 014410 (2012).
[38] Y. Konishi, Z. Fang, M. Izumi, T. Manako, M. Kasai, H. Kuwahara, M. Kawasaki, K. Terakura, and Y. Tokura, J. Phys. Soc. Jpn. **68**, 3790 (1999).
[39] L. Marín, L. A. Rodríguez, C. Magén, E. Snoeck, R. Arras, I. Lucas, L. Morellón, P. A. Algarabel, J. M. De Teresa, and M. R. Ibarra, Nano Lett. **15**, 492 (2015).
[40] M. Sharma, J. Gazquez, M. Varela, J. Schmitt, and C. Leighton, Phys. Rev. B **84**, 024417 (2011).
[41] Y. Takamura, R. V. Chopdekar, E. Arenholz, and Y. Suzuki, Appl. Phys. Lett. **92**, 162504 (2008).
[42] A. K. Pradhan, D. Hunter, T. Williams, B. Lasley-Hunter, R. Bah, H. Mustafa, R. Rakhimov, J. Zhang, D. J. Sellmyer, E. E. Carpenter, D. R. Sahu, and J.-L. Huang, J. Appl. Phys. **103**, 023914 (2008).
[43] G. Saint-Girons, R. Bachelet, R. Moalla, B. Meunier, L. Louahadj, B. Canut, A. Carretero-Genevrier, J. Gazquez, P. Regreny, C. Botella, J. Penuelas, M. G. Silly, F. Sirotti, and G. Grenet, Chem. Mater. **28**, 5347 (2016).